JOURNAL OF GEOPHYSICAL RESEARCH, VOL. 115, A07312, doi:10.1029/2009JA015100, 2010

Ionization sources in Titan's deep ionosphere

Marina Galand,[1,2] Roger Yelle,[3] Jun Cui,[1] Jan-Erik Wahlund,[4] Véronique Vuitton,[5] Anne Wellbrock,[6] and Andrew Coates[6]

Received 15 November 2009; revised 14 January 2010; accepted 4 March 2010; published 15 July 2010.

[1] We analyze a multi-instrumental data set from four Titan encounters by the Cassini spacecraft to investigate in detail the formation of the ionosphere. The data set includes observations of thermospheric and ionospheric species and suprathermal electrons. A model describing the solar and electron energy deposition is used as an organizing element of the Cassini data set. We first compare the calculated secondary electron production rates with the rates inferred from suprathermal electron intensity measurements. We then calculate an effective electron dissociative recombination coefficient, applying three different approaches to the Cassini data set. Our findings are threefold: (1) The effective recombination coefficient derived under sunlit conditions in the deep ionosphere (<1200 km) is found to be independent of solar zenith angle and flyby. Its value ranges from 6.9×10^{-7} cm^3 s^{-1} at 1200 km to 5.9×10^{-6} cm^3 s^{-1} at 970 km at 500 K. (2) The presence of an additional, minor source of ionization is revealed when the solar contribution is weak enough. The contribution by this non-solar source—energetic electrons most probably of magnetospheric origin—becomes apparent for secondary electron production rates, due to solar illumination alone, close to or smaller than about 3×10^{-1} cm^{-3} s^{-1}. Such a threshold is reached near the solar terminator below the main solar-driven electron production peak (<1050 km). (3) Our ability to model the electron density in the deep ionosphere is very limited. Our findings highlight the need for more laboratory measurements of electron dissociative recombination coefficients for heavy ion species at high electron temperatures (especially near 500 K).

Citation: Galand, M., R. Yelle, J. Cui, J.-E. Wahlund, V. Vuitton, A. Wellbrock, and A. Coates (2010), Ionization sources in Titan's deep ionosphere, *J. Geophys. Res.*, *115*, A07312, doi:10.1029/2009JA015100.

1. Introduction

[2] Titan's ionosphere was first detected by the Voyager 1 radio occultation [*Bird et al.*, 1997] but whether it is produced primarily by solar radiation or electron precipitation from Saturn's magnetosphere has been under debate for several decades [e.g., *Nagy and Cravens*, 1998]. On the one hand, Titan is located ten times further from the Sun than the Earth, which implies a solar flux one hundred time less at Titan than at Earth. On the other hand, Titan is, most of the time, within Saturn's magnetosphere where it undergoes intense bombardment from energetic particles. In addition, the magnetospheric forcing at Titan is complicated by the variation of the angle between the solar direction and the co-rotating plasma direction. Unlike at Venus, where the dayside ionosphere corresponds to the ram side of the induced magnetosphere, at Titan the magnetospheric ram location varies with local time, as Titan rotates around Saturn. This yields a complex and dynamic magnetospheric forcing and magnetic field configuration for Titan's ionosphere. It is therefore not surprising that in the pre-Cassini era, it was not clear which source of ionization was dominant on the dayside. Additional sources for the formation of ions in Titan's atmosphere include a fraction of the pickup ions freshly produced from Titan's upper atmosphere, which precipitate back especially on Saturn-facing side of Titan [*Tseng et al.*, 2008] and deposit their energy primarily above 1100 km [*Michael and Johnson*, 2005], meteorites contributing near 700 km altitude [e.g., *Ip*, 1990; *English et al.*, 1996; *Molina-Cuberos et al.*, 2001] and cosmic rays which cause ionization near 65 km [e.g., *López-Moreno et al.*, 2008].

[3] Besides remote sensing observations from radio occultations [*Kliore et al.*, 2008] and from UV imaging spectrograph [e.g., *Ajello et al.*, 2008], the Cassini spacecraft has provided a wealth of in situ measurements on Titan's upper atmosphere during close flybys of the moon. The data sets that provide the best constraint on Titan's ionosphere come from the Langmuir Probe (LP), a subsystem of the Cassini Radio and Plasma Wave Science (RPWS) experiment, the

[1]Department of Physics, Imperial College London, London, UK.
[2]Center for Space Physics, Boston University, Boston, Massachusetts, USA.
[3]Lunar and Planetary Laboratory, University of Arizona, Tucson, Arizona, USA.
[4]Swedish Institute of Space Physics, Uppsala, Sweden.
[5]Laboratoire de Planétologie de Grenoble, Université Joseph Fourier, Grenoble, France.
[6]Mullard Space Science Laboratory, University College London, Surrey, UK.

0148-0227/10/2009JA015100

Ion and Neutral Mass Spectrometer (INMS), the Electron Spectrometer sensor (ELS), a sub-system of the Cassini Plasma Spectrometer (CAPS), and the Cassini Dual-Technique Magnetometer (MAG). For the first, close flyby TA of Titan by Cassini, Cravens et al. [2005] calculated the electron density using a suprathermal electron transport model combined with a photochemical, ionospheric model, both driven by the INMS N_2 and CH_4 densities. They compared the computed values with the RPWS/LP electron density measurements [*Wahlund et al.*, 2005]. They found that solar radiation contributes to two-thirds of the maximum electron density on the inbound, dayside path and attributed the remaining contribution to electron precipitation. More recently, *Robertson et al.* [2009] applied the same method to T17 and T18 and found that solar photons are the main energy source for solar zenith angles (SZA) up to 100° above 1000 km. Furthermore, *Galand et al.* [2006] combined data from INMS, RPWS/LP, and CAPS/ELS acquired during TA with a suprathermal electron transport model and an ionospheric model solving the thermal electron energy equation. They demonstrated that for the two locations studied (at altitudes of 1220 km (SZA of 82°) and 1350 km (SZA of 74°)) the main energy source upon Titan's ionosphere was solar radiation. Finally, *Ågren et al.* [2009] analyzed a large sample of RPWS/LP electron density data set and found that the observed ionospheric peak along the Cassini trajectory is strongly dependent on the SZA. The magnitude of the peak decreases and its altitude increases with increasing SZA on the dayside and, as anticipated, well beyond the terminator (up to 110° SZA).

[4] On the nightside, the analysis of T5 and T21 flybys by *Ågren et al.* [2007] and *Cravens et al.* [2009] suggests that precipitation by energetic electrons may be the main source of Titan's ionosphere. In particular, *Cravens et al.* [2009] found a strong correlation between the suprathermal electron flux and the short-lived CH_5^+ ion density during the T5 flyby. This finding cannot however be generalized, as the magnetospheric electron and ion fluxes measured during T5 were unusually high compared with all other encounters [*Cravens et al.*, 2009]. At lower altitudes, *Cravens et al.* [2008] and *Shah et al.* [2009] suggested that precipitation of energetic protons and oxygen ions from Saturn's magnetosphere could be a significant source of ionization, with production rate peaking below 1000 km. Furthermore, *Cui et al.* [2009b] proposed that transport and survival of ions from the dayside ionosphere into the nightside contributed to the production of heavy ions well into darkness. This scenario has been supported by a multi-instrumental study combining INMS, RPWS/LP, and MAG data set from nine close encounters of Cassini with Titan [*Cui et al.*, 2010]. This study identified an ion outflow at the dayside and an ion inflow at the nightside of Titan.

[5] While Titan's dayside ionosphere, in particular the main ionospheric peak, has been shown to be primarily controlled by solar radiation, the goal of the present study is to analyze in detail Titan's ionospheric density profiles, to identify the presence of any additional ionization sources and to assess their contributions. Though we extend our analysis up to 1600 km, the prime focus here is the deep ionosphere below 1200 km where transport and diffusion can be neglected [e.g., *Ma et al.*, 2006; *Krasnopolsky*, 2009]. In order to identify the sources of ionization, we derive electron production rates and effective electron dissociative recombination coefficients through different approaches applied to a multi-instrumental data set. This data set includes thermal and energetic particle in situ measurements down to an altitude of 960 km, minimum altitude reached by Cassini during the selected flybys. An energy deposition model is used as the organizing element for the data set. The Cassini flybys and related data set are presented in section 2, followed by a description of the model in section 3.1 and the approaches applied to the data set in section 3.2. For solar-controlled ionospheric regions, the derived electron production rates and the recombination coefficients are presented in sections 4.1 and 4.2, respectively, while section 5 focuses on magnetospheric-controlled regions. Our findings are summarized and discussed in section 6.

2. Cassini Data Set

[6] Four close flybys of Titan, referred as T18, T32, T39, and T40 in the Cassini project terminology, have been selected for the present study of Titan's sunlit ionosphere. The criteria of selection are driven by the multi-instrumental aspect of the study focusing on the deep (<1200 km), sunlit ionosphere of Titan. As a result, they include the availability of useable data sets from INMS, RPWS/LP, and CAPS/ELS at SZA less than 110° for a large part of the flyby, and a close flyby with a closest approach (CA) altitude less than 1100 km. The characteristics of the selected flybys are summarized in Figure 1. Titan was moving away from southern hemisphere summer solstice with a solar declination varying from −15.6° for T18 (September 23, 2006), −11.8° for T32 (June 13, 2007), to −9.2° for T39 (December 20, 2007) and −8.7° for T40 (January 5, 2008). All the Cassini measurements used here have been reduced using standard techniques previously described in the literature: *Ågren et al.* [2009] for RPWS/LP; *Yelle et al.* [2008] for INMS neutral data; *Cui et al.* [2009b] for INMS ion data; and *Lewis et al.* [2009] for CAPS/ELS. The resultant data are displayed in Figures 2, 3, and 4. For science issues to be discussed, note from Figures 2–4 the following:

[7] 1. The dayside electron density peaks show a strong dependence in SZA (see Figure 2), as already pointed out by *Ågren et al.* [2009]. For instance, the magnitude of the peaks at T39 and T40 is significantly larger, and their altitude lower, than those of the peaks observed at T18 and T32 and associated with regions closer to the terminators (see Figure 1c). At T18, the outbound path is associated with smaller SZA values than the inbound path. This yields a larger magnitude and a lower altitude for the electron density peak at outbound than at inbound. However, the geometry of the flyby is critical in interpreting the ionospheric data set [*Cui et al.*, 2009b]. The electron density observed along the path can differ significantly from the profile along the local vertical, especially at large SZA, as attested by the difference between inbound and outbound electron densities at T18.

[8] 2. Unlike the electron density in the peak region, the electron temperature is not strongly correlated with SZA. It is instead driven by the complex configuration of the magnetic field lines [*Galand et al.*, 2006]. We have derived a polynomial of degree 1 which best fits in the least-squares sense the electron temperature data set associated with the four selected

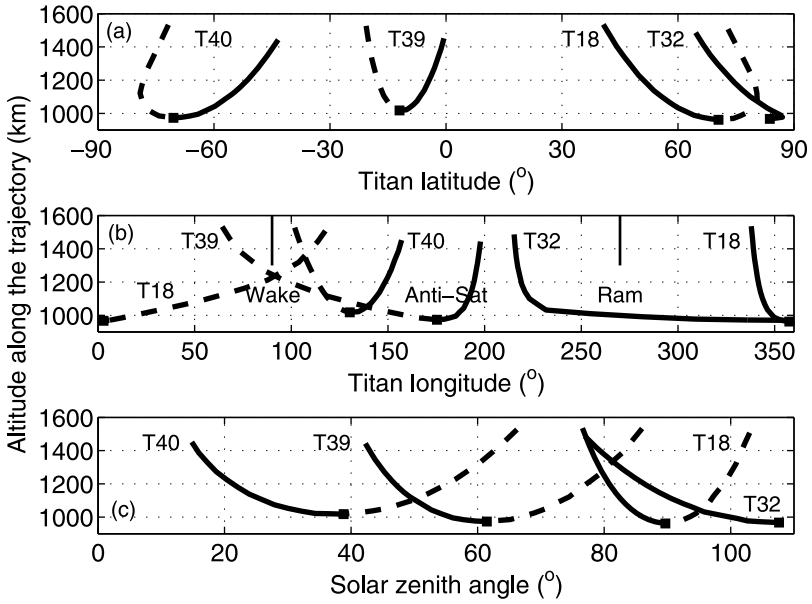

Figure 1. Characteristics of the four selected Cassini flybys. Altitude along the trajectory versus (a) latitude, (b) longitude, and (c) solar zenith angle (SZA). The dashed lines correspond to the inbound part of the trajectory, the solid lines, to the outbound part, and the filled square, to closest approach. Only T32 outbound is considered, as the rest of the trajectory is on the nightside.

flybys, as shown in Figure 3a. This fit is used as input to the suprathermal electron transport model (see section 3.1).

[9] 3. Figure 3b illustrates the increasing complexity of the ionospheric composition with lower altitudes and the role that Titan's ionosphere is anticipated to play as the source for the aerosols detected at lower altitudes [e.g., *Coates et al.*, 2007; *Vuitton et al.*, 2008]. The mean ion mass values derived from INMS should however be viewed as a lower limit in the deep ionosphere. The INMS instrument cannot detect ions of masses above 100 amu, which become increasingly abundant towards lower altitudes with fraction reaching 50–70% of

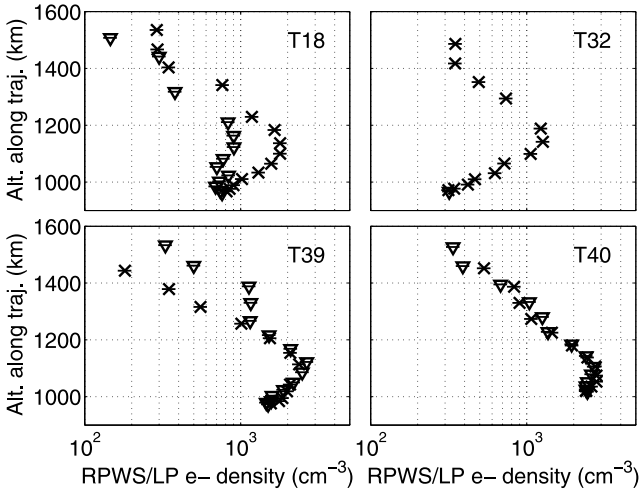

Figure 2. Ionospheric electron density (triangles for inbound and crosses for outbound) derived from RPWS/LP observations for the four selected flybys plotted as a function of the altitude along the trajectory. The ±10% uncertainty is shown with horizontal, solid lines.

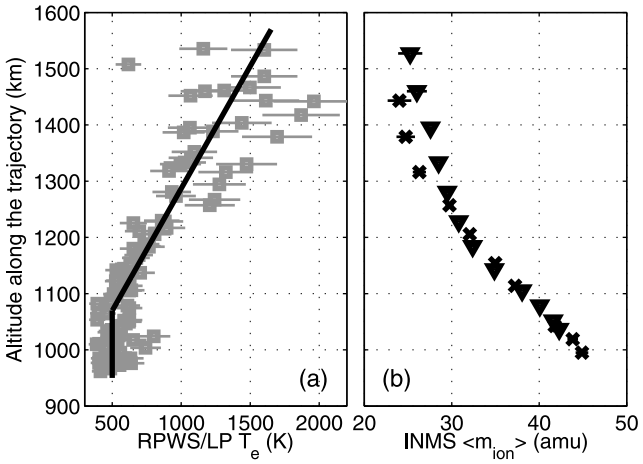

Figure 3. (a) Ionospheric electron temperature derived from RPWS/LP data set for the four selected flybys, plotted in grey as a function of the altitude along the trajectory. The ±15% uncertainty is shown with horizontal, solid lines. The solid, thick black line represents a linear fit to the data: Te[K] = 2.3 × z[km] – 1960, above 1070 km. Below, Te = 500 K. (b) Mean ion mass derived from INMS ion observations (positive ions with masses below 100 amu) for T39 outbound (crosses) and T40 inbound (triangles) plotted as a function of the altitude along the trajectory. Note that the mean ion mass derived from INMS observations is sensitive to the spacecraft potential V_{SC}. Though V_{SC} is observed by RPWS/LP, its value at the location of INMS is uncertain. We therefore only use the ion mass from the two paths for which V_{SC} derived from RPWS/LP have values within 20% of the default −0.5 V. The error related to the counting statistics ($\pm 1\sigma$) is shown with horizontal, solid lines which are often smaller than the symbol size. It is less than 1.2%.

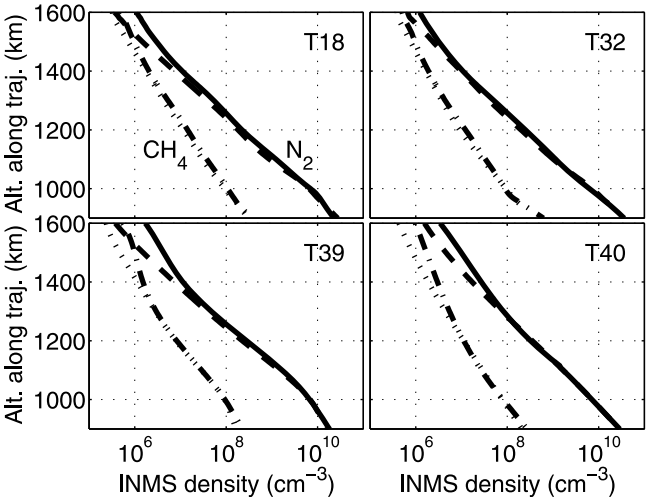

Figure 4. Altitude profile of the density of N_2 (dashed lines for inbound and solid lines for outbound) and CH_4 (dotted lines for inbound and dash-dotted lines for outbound) derived from INMS observations for the four selected flybys.

the total plasma number density in the 950–1000 km range [*Wahlund et al.*, 2009; *Crary et al.*, 2009].

3. Multi-instrumental Approach

[10] An energy deposition model, described in section 3.1, is used to link the multi-instrumental data set presented in section 2 and to calculate effective recombination coefficients, as illustrated in Figure 5. Three different approaches are applied to derive values for the effective recombination coefficient, as explained in section 3.2. Comparison of the results based on these three approaches is discussed in sections 4 and 5.

3.1. Energy Deposition Model

[11] We have solved the Beer-Lambert law for calculating the absorption of solar photons for each of the four selected flybys and solved the Boltzmann equation for calculating the transport and energy degradation of suprathermal electrons, using the model described by *Galand et al.* [2006]. The primary (by photoionization) and secondary (by electron-impact ionization) production rates are derived. The N_2 electron impact cross section has been updated based on *Shemansky and Liu* [2005], *Itikawa* [2006], and *Tian and Vidal* [1998]. The ionospheric electron temperature and the atmospheric neutral densities are derived from the RPWS/LP and INMS in situ observations (see Figures 3a and 4).

[12] The solar flux at the top of the atmosphere is based on the measurements of the Thermosphere Ionosphere Mesosphere Energetics and Dynamics (TIMED)/Solar EUV Experiment (SEE) extrapolated to Saturn [*Woods*, 2008; *Galand et al.*, 2009, and references therein]. For each case the solar flux for the day of the flyby was used. The 2006–2008 period corresponds to low solar activity. At Earth, the solar index $F_{10.7}$ was below 100 with values ranging from 65 to 95 for a month around each of the flybys. The solar variability of the solar flux extrapolated at Saturn between the different flybys, using T40 as the reference, is plotted in Figure 6. The square of the Sun-Saturn distance accounts for less than 2.5% of the variability. Above 40 nm the ratio is less than 20% except around 60 nm. The latter is related to an instrumental effect but does not affect significantly the ionization rates in an upper atmosphere, as pointed out by *Galand et al.* [2009]. Larger variability is found shortward of 40 nm, in particular in the soft X-ray region as anticipated, reaching up to 70%.

[13] The calculation of the suprathermal electron transport is performed along the local vertical. It is repeated for 14 locations of the Cassini spacecraft along the path for each of the flybys. Assuming vertical magnetic field lines is valid here as we are focusing on the total ionization rate under sunlit conditions. Under such conditions with solar input

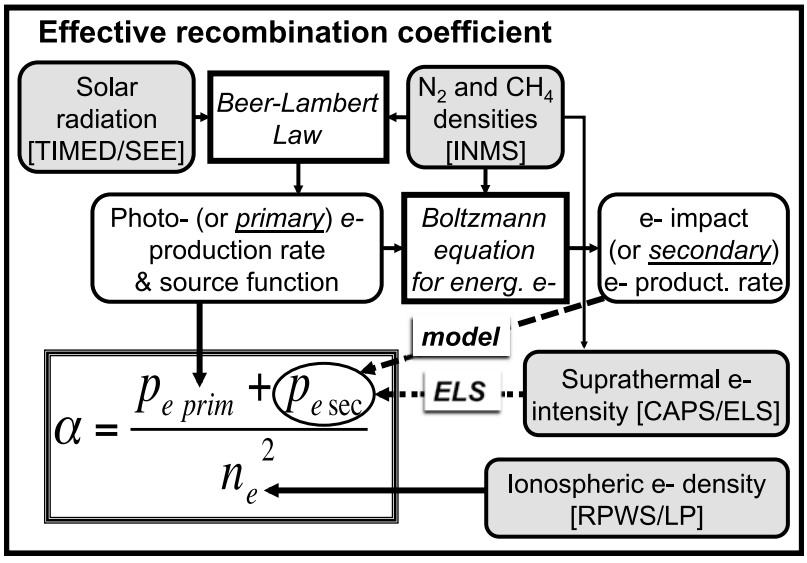

Figure 5. Schematic illustrating the assessment of the "model" and "ELS" effective recombination coefficients, α_{model} and α_{ELS}, respectively, using Cassini multi-instrumental data set binded by the energy deposition model (see section 3).

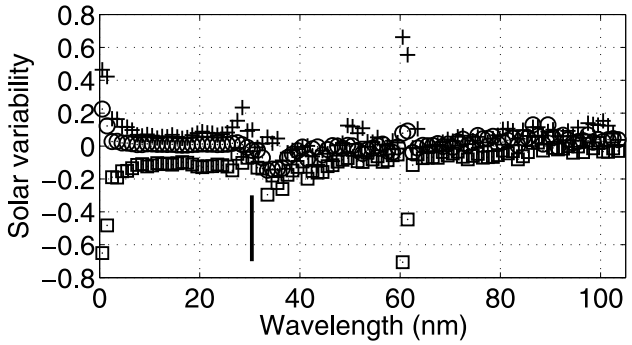

Figure 6. Solar variability between T18 (September 23, 2006) and T40 (January 5, 2008) (pluses), T32 (June 13, 2007) and T40 (squares), and T39 (December 20, 2007) and T40 (circles). The solar variability is defined as the solar flux ratio between two flybys minus one, that is, the relative variation. The solar fluxes used are derived from the TIMED/SEE extrapolated to Saturn. The square of the Sun-Saturn distance contributes to less than 2.5% of the ratios. The vertical, thick bar corresponds to the wavelength of the strong HeII (30.4 nm) solar line.

only, the transport of suprathermal electrons starts to have a significant effect on the secondary electron production rate only above about 1200–1250 km. At 1200 km (1250 km), the solution of the Boltzmann equation assuming local approximation (no transport) yields a secondary electron production rate which is less than 15% (40%) different from the one derived with transport included. The difference in secondary electron production rate between the two approaches reaches smaller values at lower altitudes. For T39 and T40, the trajectory of Cassini is actually such that photoionization is the dominant ionization source over the whole flyby. For T18 and T32 outbound, the primary production through photoionization dominates the electron production above 1100 km, while the secondary electron production rate difference between the local approximation and the transport case is within 10% below 1100 km (see section 4.1). Calculation of the transport of the suprathermal electrons along the local vertical under sunlit conditions is therefore justified for the present study focusing on the recombination coefficient derived from the total electron production rate.

3.2. Calculation of Effective Recombination Coefficients

[14] We assume local photochemical equilibrium for thermal ions and electrons. The production sources include photoionization, suprathermal electron-impact ionization, and ion-neutral chemical reactions. For light ions, the loss processes are primarily reactions with neutral species yielding the production of heavier ions, whereas for heavy ions and a few atypical light ion species, such as NH_4^+, the loss processes are dominantly electron dissociative recombination [*Vuitton et al.*, 2007; *Cui et al.*, 2009a]. Adding the continuity equations for all ion species together yields:

$$P_e(z) = \sum_i \alpha_i(z) \times N_i(z) \times N_e(z) \quad (1)$$

with P_e, the production rate reduced to photoionization (or primary ionization) and electron-impact ionization (or secondary ionization)—keeping in mind that double or triple ionizations are minor compared with single-electron ionization. N_i and N_e are the density of the ion species i and the density of electrons, respectively, α_i, the electron dissociative recombination coefficient associated with the ion species i, and z, the altitude. Equation (1) can be re-written as follows:

$$\alpha(z) = P_e(z) \times (N_e(z))^{-2} \quad (2)$$

with α, the effective recombination coefficient, defined as:

$$\alpha(z) = \sum_i \alpha_i(z) \times \frac{N_i(z)}{N_e(z)} \quad (3)$$

[15] We have applied three approaches for estimating the effective recombination coefficient α from the Cassini data set. The first two approaches are based on relation (2) and use the electron density from RPWS/LP presented in Figure 2. Figure 5 illustrates how the two recombination coefficients, α_{model} and α_{ELS}, are derived. For the "model" approach, both the primary and secondary electron production rates are calculated using the energy deposition model described in section 3.1. For the "ELS" approach, while the primary production rates are derived from the Beer-Lambert law (see section 3.1), the secondary production rates are obtained from the suprathermal electron intensities measured by CAPS/ELS as follows:

$$P_e^{ELS}(z) = 4\pi \sum_n N_n(z) \int_{E_n^{ioni}}^{E_{\max}} \sigma_n^{el}(E) \times I_e^{ELS}(E,z) \times dE \quad (4)$$

with N_n, the INMS-derived thermospheric density of species n at altitude z, I_e^{ELS}, the ELS-derived intensity of electrons at energy E at altitude z, averaged over anodes 4 to 6—the least affected by the wall effect [*Young et al.*, 2004]—(in $cm^{-2}\ s^{-1}\ eV^{-1}\ sr^{-1}$), E_n^{ioni}, the non-dissociative single-ionization threshold, and σ_n^{el}, the total electron-production cross section for species n ionized by electrons of energy E.

[16] The third approach which assesses the effective recombination coefficient α_{INMS} is based on relation (3) where the individual recombination coefficients α_i are taken from *Vuitton et al.* [2007]. Recombination coefficients for CH_3CNH^+ and $C_2H_3CNH^+$ have been updated with values of $8.1 \times 10^{-7}\ cm^3\ s^{-1}$ [*Vigren et al.*, 2008] and $1.8 \times 10^{-6}\ cm^3\ s^{-1}$ [*Vigren et al.*, 2009], respectively. The ion composition is inferred from the INMS ion analysis (see section 2). We have chosen this approach instead of using a recombination coefficient based on a detailed ionospheric model [e.g., *Vuitton et al.*, 2007; *Cui et al.*, 2009b] in order to reduce the number of uncertainties associated with the complex chemistry occurring in Titan's deep ionosphere.

[17] Finally, the individual recombination coefficients, α_i, are dependent on the electron temperature T_e:

$$\alpha_i(z) = \alpha_{i0}(z) \times \left(\frac{T_e(z)}{T_{e0}(z)}\right)^{\beta_i} \quad (5)$$

where α_{i0} is the recombination coefficient of the ion species i at the reference electron temperature T_{e0} and β_i is taken from *Vuitton et al.* [2007] with values close to −0.7 for most spe-

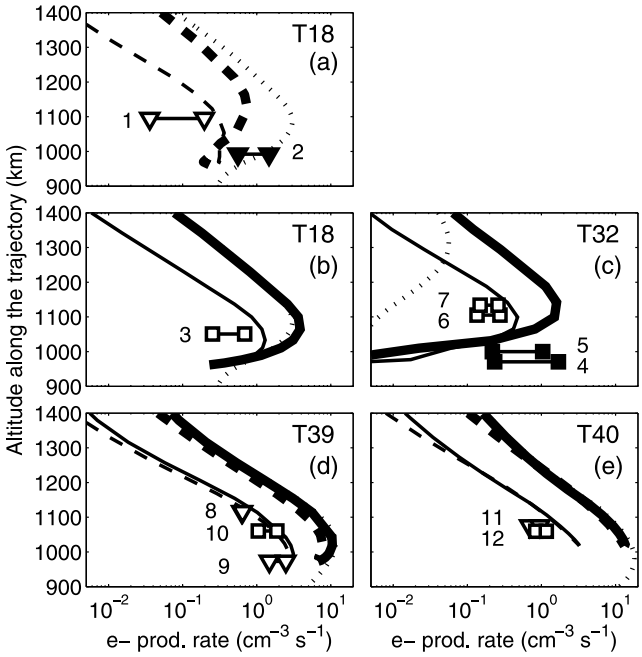

Figure 7. Calculations of the primary (thick lines) and secondary (thin lines) electron production rates along the trajectory of the Cassini spacecraft for the four selected flybys. The inbound path is shown as dashed lines and the outbound, as solid lines. For T18, the inbound and outbound paths are presented separately in Figures 7a and 7b for clarity. The triangle (inbound) and square (outbound) symbols show the secondary production rates derived from the CAPS/ELS electron intensities (see relation (4)). The range of the production rate associated with each CAPS/ELS case corresponds to two different upper limits for the energy cutoff (see text). The CAPS/ELS cases are identified with a number from 1 to 12 allocated by chronological order (see Table 1). The open symbols are associated with spectra exhibiting a sharp peak at 24.1 eV, while those filled with black are associated with spectra for which this peak is absent (see Figure 8). For reference, the calculated vertical profiles of the total (primary and secondary) electron production rates at CA are shown in dotted lines and correspond to SZA of (a and b) 89°, (c) 107°, (d) 61°, and (e) 38°. For these curves, the y-axis represents the altitude along the local vertical at CA and not the altitude along the trajectory.

cies. We assume that this temperature dependence also holds for the effective recombination coefficient α with β taken equal to −0.7. In order to be able to compare recombination coefficients derived from different flybys at a given altitude or at a given mean ion mass, all the recombination coefficients presented in section 4 and section 5 have been adjusted to the reference temperature of 500 K—representative of the deep ionosphere, as shown in Figure 3a—from the value observed by RPWS/LP at that location.

4. Solar Contribution to Titan's Ionosphere

4.1. Electron Production Rates

[18] Figure 7 shows the calculated primary (thick lines) and secondary (thin lines) electron production rates along the trajectory from inbound (dashed lines) to outbound (solid lines). Due to the extended nature of Titan's upper atmosphere, solar ionization occurs well beyond the solar terminator—as seen at T18 inbound and at T32 outbound near CA (<1150 km)—confirming earlier modeling studies [*Mueller-Wodarg et al.*, 2000; *Cravens et al.*, 2004] and recent findings based on the analysis of RPWS/LP electron density [*Ågren et al.*, 2009]. In addition, photoionization is the dominant ionization source for T39 and T40 over the whole trajectory of Cassini which flies through regions of SZA smaller than 80° below 1300 km, while electron-impact ionization rates dominate photoionization rates near CA for T18 inbound and T32 outbound, corresponding to regions of SZA larger than 80°.

[19] The secondary electron production rate becomes larger than the primary electron production rate below the altitude of penetration of 12.5 nm solar photons. Such a value is very high compared with the value of 20 nm found at Saturn for instance [*Galand et al.*, 2009]. It is explained by the presence of CH_4 in a significant amount throughout Titan's ionosphere. Solar photons in the 80–99 nm range cannot ionize N_2, but do ionize CH_4. This contribution to the primary production rate is non-negligible, as the solar flux in this spectral range reaches often values above 10^7cm^2 s^{-1} in 1 nm bins, due to the presence of the H continuum and solar lines (e.g., OII/III (83.4 nm) and CIII (97.7 nm)). In addition, this primary production peaks in the altitude region where solar photons in the 12.5–20.0 nm range deposit their energy. Below the altitude of penetration of solar photons of 99 nm, the primary production rate decreases sharply, being reduced to the ionization by solar photons of wavelength below 12.5 nm. This yields a secondary to primary electron production rate ratio larger than 1.

[20] We have compared our electron production rates with those published in Figure 6 of *Robertson et al.* [2009] for T18 outbound at 1208 km. The model used by these authors includes a two-stream electron transport model coupled with a photochemical ionospheric model in which no transport is included. The neutral density profiles they used are from INMS for T18 inbound. The solar flux is from SOLAR2000 (version 2.34) for the day of observation for wavelengths exceeding 4.2 nm and from a solar corona collisional model spectrum tuned to soft X-ray observations made by the Yohkoh observatory. At T18 outbound, the altitude of 1208 km is located well above the ionization peak (see Figure 7b) and corresponds to the altitude of deposition of solar photons in the EUV range. Over this spectral range, SOLAR2000 is based on TIMED/SEE observations, which we are using. Therefore, the solar input in *Robertson et al.* [2009] and in the present study is expected to be very similar. For the comparison, we have rerun our model using the same neutral density profiles as *Robertson et al.* [2009]. We found a value of 7×10^{-1} cm^{-3} s^{-1} for primary production rate and 9×10^{-2} cm^{-3} s^{-1} for secondary production rate of N_2^+, to be compared with 8×10^{-1} cm^{-3} s^{-1} and 7×10^{-2} cm^{-3} s^{-1}, respectively, from *Robertson et al.* [2009]. The primary and secondary production rate values between both studies are in good agreement within the difference in cross section set and uncertainty in extracting the values from Figure 6 of *Robertson et al.* [2009]. For a sanity check, we have also done a run with a solar flux turned to zero above 10 nm, keeping only the soft X-ray component of the solar flux. This

yields to a photoelectron population energetic enough to be an efficient source of ionization. From this run we have estimated the energy loss per ion produced and found a value near 37 eV on the dayside, in agreement with values found in the literature for auroral precipitation in pure N_2 atmosphere [e.g., *Rees*, 1989].

[21] The vertical profiles of the total electron production rates at CA is shown with dotted lines in Figure 7. As expected, the peak altitude increases and its magnitude decreases with increasing SZA from 38° (T40) and 61° (T39) to 89° (T18) and 107° (T32). As pointed out in section 2, the geometry of the flyby is critical for interpreting the ionospheric data set as the SZA varies over at least 20° below 1400 km during T18 and outbound T32 and over more than 40° during T39 and T40 (see Figure 1c). For large SZA (>80°), Cassini reaches the region located below the main ionization peak. In such a region, the ionization rate is strongly dependent on the SZA, as illustrated by the difference in ionization rate between the inbound and outbound paths at T18 (see Figures 7a and 7b). It is also clearly seen at T32, for which the vertical profile of the total electron production rate at CA significantly differs from the rates calculated along the Cassini trajectory (see Figure 7c). Above the main photoionization peak however, the electron production rates are not too sensitive to the SZA, as illustrated in T39 and T40 (see Figures 7d and 7e).

[22] The secondary production rates (triangles (inbound) and squares (outbound) in Figure 7) derived from the CAPS/ELS suprathermal electron intensities (see relation (4)) are compared with the model calculations. For each CAPS/ELS spectrum, two values for the electron production rates are derived. They correspond to two different upper limits for the energy cutoff. The smallest production rate was obtained by integrating the spectrum up to the energy where it reaches the 1-count level averaged over 16 s (dashed line in Figure 8). The largest production rate was obtained with an upper limit for the energy cutoff associated with the largest energy bin of CAPS/ELS. Such an approach provides two extreme cases between which the "true" value is expected to lie (assuming no significant flux beyond the ELS range). Each CAPS/ELS case is characterized in Table 1 and is identified by a number reported in Figures 7, 8, and 9c, for the sunlit cases (1–12) and in Figure 9d for the darkside cases (13–15).

[23] In order to confirm our analysis of the penetration of solar photons, we have checked for which cases the CAPS/ELS spectra exhibit a sharp peak at 24.1 eV over the central three anodes. The value of 24.1 eV corresponds to the energy of photoelectrons produced by ionization of N_2 by the dominant HeII (30.4 nm) solar line yielding the production of N_2^+ in the A state (threshold energy of 16.7 eV). Such a peak is an unambiguous photoelectron signature and has been already identified in Titan's dayside ionosphere during the first close flyby of Titan by Cassini [*Galand et al.*, 2006]. In Figure 7, the open symbols correspond to cases for which the HeII photoelectron signature was detected, while the symbols filled with black are cases for which the peak was not present over the whole range of anodes. Figure 8a shows spectra associated with the former group, while Figure 8b shows spectra associated with the latter group. The vertical bar represents the critical energy of 24.1 eV. For the cases for which the CAPS/ELS observations occurred above the altitude of penetration of the HeII (30.4 nm) solar line (given in Table 1), the CAPS/ELS spectra always exhibit an HeII photoelectron signature (cases 6–8 and 10–12) and the dominant ionization source is photoionization (as illustrated in Figure 7). For cases for which the CAPS/ELS observations occurred well below the altitude of penetration of the HeII (30.4 nm) solar line—at least 100 km below—the CAPS/ELS spectra consistently show no HeII photoelectron signature (cases 2, 4, and 5). However, for cases for which the CAPS/ELS observations occurred below but close to the altitude of penetration of the HeII (30.4 nm) solar line—less than 100 km below—the photoelectron signature is detected (cases 1, 3, and 9). Calculations of the suprathermal electron intensity confirm that the photoelectron signature is apparent down to about 100 km below the altitude of penetration of the HeII solar line. While the electron production rate associated with the absorption of HeII solar line reaches a maximum at the penetration altitude, the flux of 30.4 nm solar photons is not equal to zero. Full absorption of the solar flux at 30.4 nm occurs about 100 km below the penetration altitude. It should also be noted that the penetration altitude is sensitive to uncertainties in modeling input. For instance, a reduction of the neutral density by 15% for case 1 decreases the altitude of penetration of the HeII solar line by 45 km. In addition, the CAPS/ELS spectra are the result of measurements over 16 s which corresponds to a range of altitudes, especially away from closest approach (e.g., 30 km for case 1).

[24] Another interesting finding is that when the secondary electron production rate P_e* calculated assuming solar input alone is large enough, larger than about 3×10^{-1} cm^{-3} s^{-1} (cases 3, 6–12), the secondary electron production rate P_e^{ELS} derived from CAPS/ELS spectra is close to P_e*. When P_e* is below 3×10^{-1} cm^{-3} s^{-1}, the secondary electron production rate P_e^{ELS} derived from CAPS/ELS spectra can be significantly larger than the total electron production rate calculated with solar input alone, which is seen for cases 2, 4, and 5. In summary, when the secondary electron production rate due to solar radiation is large enough, above a certain threshold, no other sources are detected. When it is below this threshold, the presence of a non-solar population of suprathermal electrons, additional source of ionization, may be revealed. In other words, there is a minor contribution to ionization, most probably from magnetospheric electrons, that only becomes apparent when the solar source is weak.

[25] Finally, we find that for cases 1, 3, 6, 7, 11, and 12, the secondary electron production rate P_e^{ELS} is smaller than the calculated P_e*, by 35 to 50% when the upper limit for the energy cutoff for P_e^{ELS} is chosen to be the highest energy bin of CAPS/ELS (26 keV), well above the energy of the photoelectrons induced by soft X-ray (0.1–10 nm) solar photons. Such a discrepancy, not seen during T39 (cases 8–10) may be due to several factors: (1) uncertainty in the solar flux at Saturn estimated to be 20% at most in the EUV (10–100 nm), spectral range most critical near the main production peak, (2) uncertainty in photo- and electron-impact cross sections (15%) (3) uncertainty in the CAPS/ELS. The counting statistics error yields an uncertainty of 8% for T40 and up to 13% for T32, while the uncertainty associated with the absolute

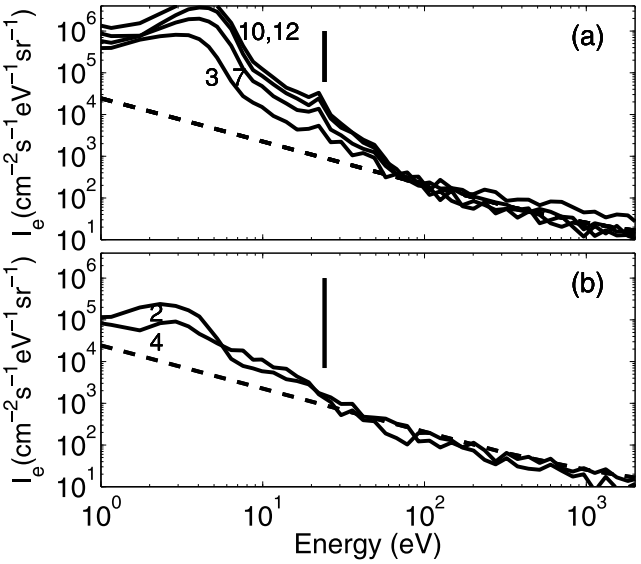

Figure 8. (a) Electron intensity as a function of the electron energy, observed by CAPS/ELS, for cases 3, 7, 10, and 12, as defined in Table 1 and identified in Figure 7. (b) Same as Figure 8a but for cases 2 and 4, as defined in Table 1 and identified in Figure 7. The spectra shown here are the average of 8 samples (16 s) over anodes 4 to 6. They have not been corrected for the spacecraft potential which significantly affects the spectrum primarily below 10 eV. The dashed line is associated with the 1-count level averaged over 8 samples (16 s). The vertical, thick bar corresponds to an energy of a photoelectron produced by the ionization of N_2 by HeII (30.4 nm) solar photons to produce N_2^+ in the A state (24.1 eV). A sharp peak, signature of HeII-related photoelectrons, is detected at this energy—within the energy resolution of the CAPS/ELS (17%) and uncertainty in the spacecraft potential (near 0.5 eV for T39 and T40 and <2 eV for T18 and T32)—in the spectra shown in Figure 8a but not in the spectra shown in Figure 8b.

calibration and the error associated with the uncertainty in the spacecraft potential are estimated to be about 10% and up to 20%, respectively. We checked that the atmospheric neutral densities do not play a significant role here, as they affect in a similar way both the modeled and CAPS/ELS secondary electron production rates. They however affect the absolute values of the rates. If the neutral densities are multiplied by a factor of 2, the electron production rate peaks move up. Their magnitudes increase with a relative difference from 5% for T18 to 20% for T32 for primary production rates and from 15% for T18 to 45% for T40 for secondary production rates.

4.2. Effective Recombination Coefficients

[26] The recombination coefficients, α_{model}, α_{INMS}, and α_{ELS}, derived as described in section 3.2, are presented in Figures 9a–9c for sunlit conditions: Figures 9a and 9b on the dayside (SZA < 85°) and in Figure 9c near the terminator (85° < SZA < 110°). All the recombination coefficients shown have been adjusted to an electron temperature of 500 K applying relation (5), as explained in section 3.2. The mean ion mass derived from the INMS data set and presented for T39 outbound and T40 inbound only should be viewed as qualitative (see section 2). As a consequence, quantitative information in section 4.2 is only provided for Figures 9a and 9c.

4.2.1. Dayside Ionosphere

[27] On the dayside (SZA < 85°), α_{model} at low altitudes, below 1200 km (or high mean ion mass, above 32 amu) is well organized, independently of the flyby selected and SZA (see Figures 9a and 9b). A fit to the data set provides the following altitude dependence:

$$\alpha(z) = 10^{\left(8.82\times10^{-6}\times z_0^2 - 5.56\times10^{-3}\times z_0 - 5.405\right)} \quad (6)$$

where α, given at 500 K, is in cm^3 s^{-1} and $z_0 = z - 1000$ with z, the altitude in km (970 < z < 1200 km).

[28] It is not surprising to find an effective recombination coefficient in the dayside deep ionosphere independent of the flyby selected and SZA. In this region, solar photons are the main ionization source (see Figure 7). Furthermore, the assumption of a photochemical regime is a good approximation [e.g., *Ma et al.*, 2006]. In addition, the ion mass increases with lower altitudes (see Figure 3b) yielding the increasing abundance of heavier hydrocarbons (e.g., *c* − $C_3H_3^+$, HC_3NH^+), whose main loss is through electron dissociative recombination [e.g., *Vuitton et al.*, 2007; *Cui et al.*, 2009b].

[29] The same trend is found for the effective recombination coefficient in all three approaches, "*model*", "*INMS*", and "*ELS*" in the deep ionosphere (z < 1200 km or m_i > 32 nm): an increase of the recombination coefficient with lower altitudes (see Figure 9a) or with larger mean ion mass (see Figure 9b). For clarity, α_{ELS} has not been added to Figures 9a and 9b, owing to close values to α_{model} for SZA < 85° (see Figure 7). The trend found for α is explained by a change in composition from $HCNH^+$ (28 amu) as dominant species to an increase in the abundance of c-$C_3H_3^+$ (39 amu), and HC_3NH^+ (52 amu). The former has a very low recombination coefficient of 2.8×10^{-7} cm^3 s^{-1} at 300 K [*Semaniak et al.*, 2001] (2.0×10^{-7} cm^3 s^{-1} at 500 K), while the two latter ion species have a recombination coefficient of 8×10^{-7} cm^3 s^{-1} [*McLain et al.*, 2005] (6×10^{-7} cm^3 s^{-1}) and 1.5×10^{-6} cm^3 s^{-1} [*Geppert et al.*, 2004] (10^{-6} cm^3 s^{-1}), respectively (applying relation (5)).

[30] It is interesting to note that α_{INMS} differs between T39 outbound and T40 inbound above 1250 km (see Figure 9a), which corresponds to a region where the mean ion mass between these two paths also differs (m_i < 30 amu) (see Figure 3b). However, when plotted as a function of mean ion mass, α_{INMS} for both paths have very close values.

[31] The values found for α_{INMS} are however significantly lower than those obtained for α_{model}, with a ratio between α_{model} and α_{INMS} ranging from 1.6 at 1200 km to 7.1 at 1000 km. The value of α_{INMS} in the deep ionosphere may be underestimated because heavy ion species of larger masses than 100 amu become increasingly abundant in this region [e.g., *Waite et al.*, 2007; *Wahlund et al.*, 2009; *Crary et al.*, 2009]. If we assume that all the species at 1000 km are heavy hydrocarbons (>100 amu), the largest realistic value for a recombination coefficient does not exceed 2×10^{-6} cm^3 s^{-1} at 300 K (W. D. Geppert, personal communication, 2009), that is, 1.4×10^{-6} cm^3 s^{-1} at 500 K, assuming a power index β (see relation (5)) of −0.7. This would reduce the relative

Table 1. CAPS/ELS Cases in the Deep Ionosphere Below 1200 km, Away From Regions Contaminated by Negative Ions [*Coates et al.*, 2007][a]

Case	Flyby (Inbound/Outbound)	Cassini Altitude (km)	Cassini SZA (deg)	Penetration Altitude of HeII Solar Line (km)	Primary P_e ("Model") (cm^{-3} s^{-1})	Secondary P_e ("Model") (cm^{-3} s^{-1})	Secondary P_e ("ELS") (cm^{-3} s^{-1})
			Sunlit Ionosphere (SZA < 110°) (See Figures 7 and 9c)				
1	T18 (in)	1095	97	1127	6.5×10^{-1}	3.1×10^{-1}	3.6×10^{-2}–2.0×10^{-1}
2	T18 (in)	992	93	1095	2.4×10^{-1}	3.2×10^{-1}	5.6×10^{-1}–1.5×10^{0}
3	T18 (out)	1051	84	1060	3.6×10^{0}	1.3×10^{0}	2.5×10^{-1}–6.9×10^{-1}
4	T32 (out)	971	104	1272	3.8×10^{-4}	3.7×10^{-3}	2.3×10^{-1}–1.7×10^{0}
5	T32 (out)	1000	99	1186	4.6×10^{-3}	3.6×10^{-2}	2.2×10^{-1}–1.0×10^{0}
6	T32 (out)	1105	91	1097	1.6×10^{0}	4.9×10^{-1}	1.4×10^{-1}–2.8×10^{-1}
7	T32 (out)	1134	89	1086	1.6×10^{0}	4.0×10^{-1}	1.5×10^{-1}–2.6×10^{-1}
8	T39 (in)	1116	74	1032	4.0×10^{0}	8.1×10^{-1}	6.3×10^{-1}–6.4×10^{-1}
9	T39 (in)	973	63	1008	6.7×10^{0}	2.9×10^{0}	1.5×10^{0}–2.5×10^{0}
10	T39 (out)	1060	52	992	9.6×10^{0}	2.1×10^{0}	1.1×10^{0}–1.9×10^{0}
11	T40 (in)	1075	48	988	8.5×10^{0}	1.8×10^{0}	7.0×10^{-1}–9.5×10^{-1}
12	T40 (out)	1060	29	971	1.1×10^{1}	2.2×10^{0}	8.4×10^{-1}–1.2×10^{0}
			Dark Ionosphere (SZA > 110°) (See Figure 9d)				
13	T32 (in)	1145	125	0	0	0	4.4×10^{-4}–9.1×10^{-2}
14	T32 (in)	1079	122	0	0	0	1.8×10^{-3}–2.3×10^{-1}
15	T32 (in)	1007	116	0	0	0	1.2×10^{-1}–1.0×10^{0}

[a]Shown are identification number, Cassini information at the time of ELS observations, deposition altitude of the HeII (30.4 nm) solar line, and electron production rates P_e derived as explained in section 4.1.

difference between α_{INMS} and α_{model} from 86% to 65%. Uncertainties for the recombination rates are typically 20% at 300 K. In addition, the power index β is not well known. On the one hand, *McLain et al.* [2004] suggest a switch in β from −0.7 to −1.4 above 300 K, which would reduce even more the above recombination coefficient at 500 K, down to 9.8×10^{-7} cm^3 s^{-1}. On the other hand, an increase in the recombination coefficient from 8×10^{-7} cm^3 s^{-1} in the 200–300 K range to 1.6×10^{-6} cm^3 s^{-1} in the 450–500 K range have been observed for c-$C_3H_3^+$, though there is no clear explanation for it at this stage [*McLain et al.*, 2005]. More laboratory measurements and further theory for extrapolating the recombination coefficient to heavy hydrocarbons near 500 K are critically needed for providing a better constraint on α_{INMS}. Regarding α_{model}, it is proportional to the electron production rate, which depends on the INMS neutral densities, the cross sections, particularly photoabsorption and photoionization cross sections which are known within 15%. If the neutral densities are multiplied by a factor of 2, the recombination coefficient at 1200 km increases with a relative difference by 88%. At 1000 km however, the variation is significantly less with a recombination coefficient within 15% of the default value. In addition, the ±10% uncertainty on the RPWS/LP electron densities yields an uncertainty of ±20% on α_{model}. Finally, negative ions have been detected in the deep ionosphere, with densities up to 10% of the negatively charged population in the 950–1000 km range [*Coates et al.*, 2007; *Wahlund et al.*, 2009]. Their presence yields a decrease of 23% in the electron recombination coefficient in this region.

[32] At higher altitudes (above 1200 km), the recombination coefficients α_{model} are spread over a large range of values and no clear altitude dependence can be inferred. The spread can be primarily explained by transport effect and diffusion, which become dominant above 1300 km. Diffusion yields a decrease in the electron density compared with the photochemical regime, which implies an increase in recombination coefficient [*Ma et al.*, 2004, 2006]. Recently, *Cui et al.* [2010] found that the globally averaged measured electron density is smaller than the density calculated in diffusive equilibrium. They concluded that there is a global ion escape from Titan with a total ion loss rate of about 1.7×10^{25} s^{-1}. They also inferred ion outflow at the dayside and ion inflow at the nightside occurring primarily between 1300 and 1400 km and yielding a decrease and an increase, respectively, of the electron density compared with the diffusive regime. Another reason for the spread in α_{model} is additional sources of ionization, as discussed in section 5.1 for T39 inbound (open, red triangles). It should be noted that, though the electron temperature spreads over a large range at high altitudes (see Figure 3a), the effect of this spread does not significantly contribute to the spread in α_{model}, as attested by the moderate spreading of α_{INMS} (see Figure 9a).

[33] It is interesting to see a change in the slope of α_{INMS} around 1200 km (see Figure 9a) or 32 amu (see Figure 9b). It is also clearly seen in α_{model} for some of the flybys, such as for T39 outbound (red crosses), though the effect may be more pronounced at high altitudes due to the contribution of transport processes. This "elbow" shape is the result of composition changes. Near 1200 km, the most abundant species is $HCNH^+$ which has the lowest recombination coefficient (2.8×10^{-7} cm^3 s^{-1} at 300 K) among the most abundant species in Titan's ionosphere. At higher altitudes, $C_2H_5^+$ and CH_5^+ become the dominant species, while at lower altitudes, c-$C_3H_3^+$ and HC_3NH^+ become increasingly abundant. All these species have recombination coefficients close to 10^{-6} cm^3 s^{-1} at 300 K, that is, significantly larger than the coefficient for $HCNH^+$.

4.2.2. Ionosphere Near Solar Terminator

[34] Near the solar terminator (85 < SZA < 110°), above 1050 km α_{model}—shown with open blue triangles for T18 inbound and green crosses for T32 outbound—has values very close to those found on the dayside and represented by the fit (black, solid line) (see Figure 9c). Though the SZA reaches values from 95 to 100° for T18 inbound and from 85 to 95° for T32 outbound, this result is not surprising. Above 1050 km, the main ionization source is still photoionization

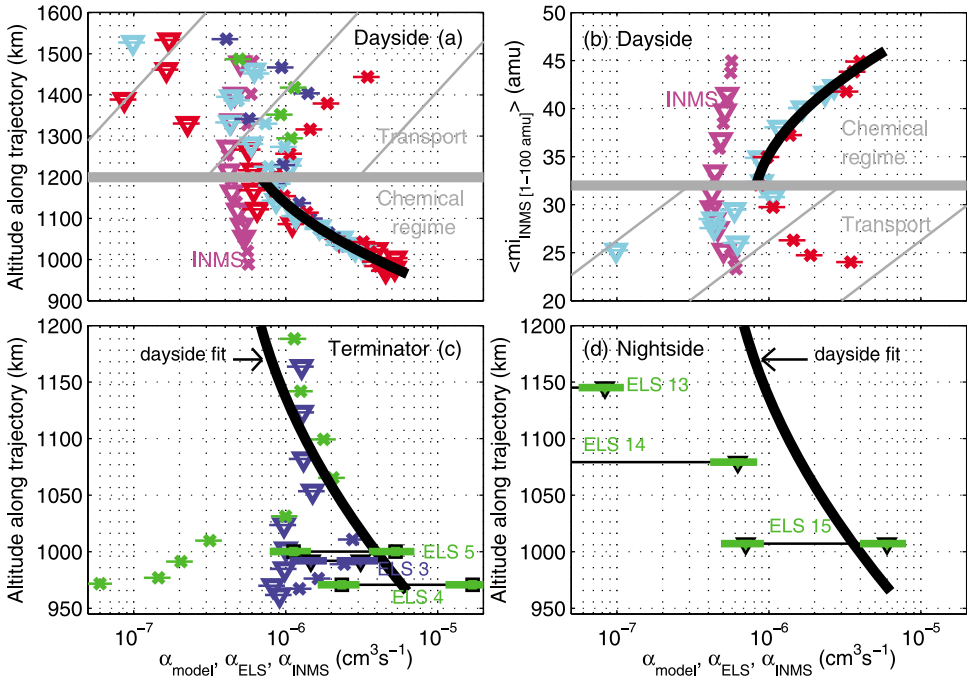

Figure 9. (a) Altitude profiles of the modeled effective recombination coefficient, α_{model}, for the four selected profiles for "dayside" conditions (sza < 85°) (T18 in blue, T32 in green, T39 in red, and T40 in cyan). Open triangles correspond to inbound and crosses to outbound. The INMS-derived effective recombination coefficient, α_{INMS}, is also shown with magenta for T39 outbound (triangles) and T40 inbound (crosses). The ELS-derived effective recombination coefficients, α_{ELS}, are not plotted for clarity, as they are very close to α_{model} due to the dominance of the primary production rate compared with the secondary rate for the SZA range considered here (see Figure 7). The thick, solid, black line represents the best fit of the modeled effective recombination coefficient, α_{model} below 1200 km (defined as relation (6)) and is also shown in Figures 9c and 9d. (b) Same as Figure 9a but using INMS-derived mean ion mass instead of the altitude along the trajectory. The thick, solid, black line represents the best fit of the modeled effective recombination coefficient, α_{model} for ion masses larger than 32 amu. The triangles are related to T40 inbound and the crosses, to T39 outbound. (c) Altitude profiles of the modeled effective recombination coefficient, α_{model}, for T18 (blue) and T32 (green) for "terminator" conditions (85° < SZA < 110°). The ELS-derived effective recombination coefficient is shown with filled symbols (triangles for inbound and squares for outbound) for T18 (blue) and T32 (green), respectively. The range of α associated with each CAPS/ELS spectra corresponds to two different upper limits for the energy cutoff (see text). Only cases 2 (filled blue triangles), 4 and 5 (filled green squares), as defined in Table 1 and identified in Figure 7 and for which the ELS-derived secondary production rates are significantly larger than the modeled ones, are presented. (d) ELS-derived effective recombination coefficient, α_{ELS}, for cases 13, 14, and 15 as defined in Table 1 (green, filled triangles) for "nightside" conditions (SZA > 110°). All the recombination coefficients have been corrected to a reference temperature of 500 K assuming a temperature-dependence coefficient β of −0.7 (see relation (5)). The error bars (colored, horizontal bars) shown for α_{model} are associated with the uncertainty in RPWS/LP electron density, while for α_{ELS} they represent both the uncertainty in RPWS/LP electron density and the counting statistics error associated with CAPS/ELS electron intensity.

(see Figure 7a for T18 inbound and Figure 7c for T32 outbound). These cases are therefore similar to the dayside cases presented in Figures 9a and 9b. Below 1050 km, α_{model} departs from the dayside fit (solid, black line). This region for which solar radiation is no longer the dominant ionization source is discussed in section 5.1.

5. Magnetospheric Electron Contribution to Titan's Ionosphere

5.1. Sunlit Ionosphere

[35] Solar radiation is the main source of ionization on the dayside (SZA < 85°). Due to large secondary electron production rates (>0.3 cm^{-3} s^{-1}) between 950 km and 1200 km, no additional ionization sources have been detected in this region during the selected flybys (see section 4.1). However, at higher altitudes the effect of non-solar forcing is seen. The electron density profile at T39 inbound exhibits an increase near 1350 km (see Figure 2). This "bump", most probably related to ionization by energetic particles (e.g., soft electrons, pickup ions), yields very low values for α_{model} for which solar radiation is assumed to be the only ionization source (red triangles in Figure 9a).

[36] In the terminator region at low altitudes (below 1050 km) the contribution of solar photons yields a secondary electron production rate below about 3×10^{-1} cm^{-3} s^{-1} and

additional sources of ionization have been revealed (see section 4.1). In the cases studied, this corresponds to a region located below the primary electron production peak—associated with the deposition of EUV (mainly HeII(30.4 nm)). It corresponds to a region where solar soft X-rays produce energetic photoelectrons. In this region, the secondary production rate (due to solar radiation only) dominates the primary production rate, as illustrated by cases 2, 4, and 5 in Figures 7a and 7c. The ELS-derived electron production rate (filled triangles in Figure 7a and filled squares in Figure 7c) is found to be larger than the secondary production rate due to solar radiation only. This implies the existence of a non-solar source of energetic electrons, most probably electron bombardment from Saturn's magnetosphere.

[37] The analysis of effective recombination coefficients supports the assumption of magnetospheric electrons as the significant, additional source of ionization. Figure 9c shows that, if solar radiation is the only ionization source, the recombination coefficient α_{model} calculated for T18 (open, blue triangles and blue crosses) and T32 (green crosses) has significantly lower values than what is found on the dayside (solid, black line). Furthermore, the range of values found for the ELS-derived recombination coefficient, α_{ELS}, derived for T18 (filled, blue triangles) and T32 (filed, green squares), at a given altitude is including (T32)—or very close to (T18)—the value obtained in that altitude on the dayside (solid, black line).

5.2. Nightside Ionosphere

[38] Though the present study focuses on the sunlit ionosphere (SZA < 110°), we examine here three additional examples extending the study towards the nightside. Figure 9d shows the ELS-derived recombination coefficient for T32 inbound (filled, green triangles) for cases 13, 14, and 15, as defined in Table 1. The range of values for each ELS case corresponds to two different upper limits of the integral over energy. The largest value corresponds to the largest energy bin of CAPS/ELS (with a central energy of 26 keV), while the smallest value corresponds to the energy at which the electron intensity becomes close to the 1-count level. In these cases, the energy corresponding to the ELS 1-count level is very small, 20 eV for cases 13 and 14 and 40 eV for case 15. While the range of values derived for α_{ELS} for case 15 includes the dayside α_{model} value at that altitude (black, solid line) (see Figure 9d), the α_{ELS} values for cases 13 and 14 are significantly lower than the values obtained on the dayside. One possible explanation for this is the contribution of transport from dayside to nightside [*Cui et al.*, 2009b, 2010]. This scenario would imply an inflow of ions from the dayside, which is not accounted for in α_{ELS}. However, no definite conclusion can be drawn at this time due to the small sample.

6. Concluding Remarks and Discussion

[39] We have analyzed a multi-instrumental data set from four close Cassini flybys of Titan originally combined using a model for deposition of solar and electron energy and assuming photochemical equilibrium. Solar radiation is the dominant ionization source between 1050 km and 1200 km, but we have unambiguously revealed the presence of suprathermal electrons of non-solar origin below 1050 km for 85° < SZA < 110°. In this region located below the peak of the photoionization production rate, the solar contribution to the electron production rates becomes low enough to enable the contribution by this additional, minor ionization source to be revealed. The most probable origin for this additional source of suprathermal electrons is Saturn's magnetosphere which closely interacts with Titan's ionosphere. Another possible source in this altitude region is solar flares, as it has been seen at other planets [e.g., *Mendillo et al.*, 2006]. The solar flux in the soft X-ray range which yields the production of energetic photoelectrons is known to be highly variable [*Neupert*, 2006]. It could have been significantly underestimated. However, extrapolating from Earth-based observations, the flybys analyzed here and made during solar minimum seem to be associated with periods of relative quiet solar X-ray activity. Energetic oxygen ions could also contribute to the production of electrons and ions, especially below 1050 km in the terminator regions [*Cravens et al.*, 2008; *Shah et al.*, 2009]. However, the relatively good agreement, within the error bars, between the recombination coefficients on the dayside and those obtained from CAPS/ELS electron fluxes for two different near-terminator flybys T18 and T32 (see Figure 9c) tends to show that, for those two flybys at least, the main additional source is energetic electrons from Titan's magnetized environment.

[40] On the dayside (SZA < 85°) we have confirmed that EUV solar radiation is the main ionization source for the ionosphere between 970 km (imposed by Cassini closest approach altitude for the selected, dayside flybys) and 1200 km. Above this altitude, non-solar ion sources become significant occasionally (e.g., T39 inbound). Such ion sources may possibly be soft electron precipitation from Saturn's magnetosphere or freshly produced pickup ions. On the nightside (SZA > 110°), due to low signal-to-noise ratio in the cases analyzed here we cannot conclude with certainty that magnetospheric electrons are important compared with other sources of ions, such as the inflow of ions from the dayside [*Cui et al.*, 2009b, 2010]. A more systematic analysis of the darkside ionosphere will be the focus of a future study.

[41] In the deep, sunlit ionosphere (below 1200 km altitude for SZA < 110°), we found that the effective recombination coefficient is independent of the SZA (see sections 4 and 5). This includes regions where non-solar sources dominate ionization (see section 5). The effective recombination coefficient however is a function of altitude, as illustrated in Figure 9a, as a result of the altitude-dependence of atmospheric composition (including minor neutrals) which drives a complex chemistry [e.g., *Vuitton et al.*, 2007]. The values obtained for the effective recombination coefficient vary from 5.9×10^{-6}cm^3 s^{-1} at 970 km to 6.9×10^{-7}cm^3 s^{-1} at 1200 km for T_e of 500 K (assuming relation (5) for the T_e-dependance connected to T_e = 500 K).

[42] We have derived a relation for the effective recombination coefficient as a function of altitude (relation (6) at 500 K combined with (5) for the T_e-dependance), which is valid in the deep, sunlit ionosphere (below 1200 km altitude for SZA < 110°). Applying the Beer-Lambert law for calculating the photoelectron production rate, it can be used for a quick assessment of the electron density from 970 km to 1200 km on the dayside (SZA < 85°) and between 1050 km and 1200 km in the terminator regions (85° < SZA < 110°). Below 1050 km near the terminators, additional sources of

ionization including magnetospheric electrons and secondary electrons under solar illumination need to be included as well. At high altitudes (>1200 km), beside additional sources of ionization, transport processes and diffusion need also to be taken into account for calculating the electron density.

[43] Comparison between α_{model} and α_{INMS} in the deep ionosphere highlights our limited knowledge of recombination coefficients and their dependence with electron temperature above 300 K. At 1200 km, the ratio between α_{model} and α_{INMS} is found to be 1.6. This implies a relative difference between the derived electron densities, Ne_{INMS} and Ne_{model}, of 26%. Based on photochemical models, *Cravens et al.* [2005] and, more recently, *Krasnoplosky* [2009] derived a value of 6×10^{-7} cm^3 s^{-1} at 300 K and 2×10^{-7} cm^3 s^{-1} at 680 K, respectively, at 1200 km. These values correspond to 4.2×10^{-7} cm^3 s^{-1} and 2.5×10^{-7} cm^3 s^{-1}, respectively, at 500 K (assuming relation (5) for the T_e-dependence). The 500 K value based on *Cravens et al.* [2005] is very close to what is found for α_{INMS} (4.3×10^{-7} cm^3 s^{-1}), while the 500 K value based on *Krasnopolsky* [2009] is even lower than these two values. The 500 K values based on both photochemical models yield an overestimation of the electron density compared with the density derived from our best estimation of the recombination coefficient, α_{model} (6.9×10^{-7} cm^3 s^{-1}). At 1000 km, *Krasnopolsky* [2009] calculated a value of 6×10^{-7} cm^3 s^{-1} at 300 K, that is, 2.5×10^{-7} cm^3 s^{-1} at 500 K (assuming relation (5) for the T_e-dependence), to be compared with the value of 3.9×10^{-6} cm^3 s^{-1} for α_{model}. This yields a ratio between α_{model} and α from *Krasnopolsky* [2009] of 10, while the ratio between α_{model} and α_{INMS} is found to be 7. This implies that the electron density derived from *Krasnopolsky* [2009] and from α_{INMS} are a factor of about three larger than the electron density inferred from α_{model}. It highlights our current, limited ability to model the electron density in the deep ionosphere. More laboratory measurements of the electron dissociative recombination rate of ion species present at Titan are needed, extending towards high temperatures (>450 K) and high masses (>100 amu).

[44] Though we have found regions where the main ionization source is magnetospheric electrons, we have not attempted here to make an estimation of the expected electron production rates induced by magnetospheric particles, which requires the knowledge of the magnetic field configuration (unlike calculations in the present study, as explained in section 3.1). The reason is twofold. There is a poor constraint on both the incident electron intensity and the configuration of the magnetic field lines which cross the trajectory of Cassini. Though CAPS/ELS measures the electron intensity before penetrating (ingress) and after having flown through (egress) Titan's ionosphere, these two measurements may not correspond to the incident intensity at each "end" of the magnetic field line along which the magnetospheric electrons are transported. Furthermore, while the MAG instrument measures the magnetic field along the trajectory of the Cassini spacecraft, the knowledge of the global magnetic field configuration in Titan's ionosphere requires modeling from MHD [e.g., *Backes et al.*, 2005; *Ma et al.*, 2006, 2009] or hybrid models [e.g., *Modolo and Chanteur*, 2008; *Simon et al.*, 2009]. Though some modeling outputs are available for T32 [e.g., *Ma et al.*, 2009; *Simon et al.*, 2009], calculations of the configuration of the magnetic field near Titan are often performed at a low spatial resolution and are not always strongly constrained.

[45] The problem could however be reversed. It is possible to derive the electron production rate associated with magnetospheric electrons from the CAPS/ELS derived rates minus the contribution by photoelectrons and their secondaries that we have calculated. For cases 4 and 5 (see Table 1 and Figure 7c), we find 2.3×10^{-1}–1.7 cm^{-3} s^{-1}, and 1.8×10^{-1}–9.6×10^{-1} cm^{-3} s^{-1}, respectively. To this range of values associated with the two extreme values for the energy cutoff for integrating CAPS/ELS intensities, an uncertainty of 30% must be added to account for the uncertainty in absolute calibration (10%) and spacecraft potential (up to 20%). Additional uncertainties include those in cross sections (15%), neutral densities, and solar flux. If the neutral density is increased by a factor 2, on the one hand the solar flux deposits its energy higher up and the resulting primary and secondary production rates associated with solar deposition are reduced. On the other hand, the CAPS/ELS-derived production rate which is proportional to the neutral density (see relation (4)) is doubled. As a result, the value obtained for the electron production rate associated with magnetospheric electrons are more than doubled, increasing to 2.7×10^{-1}–3.4 cm^{-3} s^{-1} for case 4 and to 4.0×10^{-1}–2.0×10^{-1} cm^{-3} s^{-1} for case 5. As for the solar flux, if it is increased by a factor of 2 in the soft X-ray (<10 nm), the solar-related primary and secondary production rates are doubled. However, as they only represent a small fraction of the ELS-derived production rates, the electron production rate associated with magnetospheric electrons are only reduced by 2% for case 4 and 24% for case 5. Based on electron transport calculations for a parabolic magnetic field line configuration, *Cravens et al.* [2005] derived N_2^+ production rates peaking above 1200 km for incident electron characteristics at 200 eV and below. As a result, the production rates they derived at 1000 km and below, altitudes at which we observe the magnetospheric contribution, are smaller than 10^{-2} cm^{-3} s^{-1}. Even for a vertical magnetic field configuration, 200 eV magnetospheric electrons deposit their energy primarily above 1100 km [*Cravens et al.*, 2005; *Ågren et al.*, 2007]. The production rate detected may therefore most probably be caused by magnetospheric electrons of energy larger than 200 eV. Recent calculations by *Cravens et al.* [2009] applied to T5 and T21 nightside flybys confirm that such high rates in production can be reached using as boundary conditions energy distributions based on CAPS/ELS fluxes measured in Titan's near environment and extending well above 200 eV.

[46] **Acknowledgments.** M.G. and J.C. acknowledge the support from the Science and Technology Facilities Council (STFC) through the rolling grant to Imperial College London. R.V.Y. acknowledges support from NASA grant NNX09AB58G and the Cassini project. This work was written while M.G. was on leave at Boston University. We would like to thank M. Mendillo very much for his hospitality and for many enriching discussions on ionospheric processes. We would also like to thank I. Mueller-Wodarg who led an international team on Titan aeronomy (ISSI team 106) and the International Space Science Institute (ISSI) who supported this effort. This work greatly benefited from enriching and constructive discussions during the ISSI team meetings. Finally, we are very grateful to the TIMED/SEE PI, Tom Woods, and his team for providing us with the solar flux data set and associated routines of extrapolation to planets.

[47] Masaki Fujimoto thanks the reviewers for their assistance in evaluating this paper.

References

Ågren, K., et al. (2007), On magnetospheric electron impact ionisation and dynamics in Titan's ram-side and polar ionosphere—A Cassini case study, *Ann. Geophys.*, *25*, 2359–2369.

Ågren, K., J.-E. Wahlund, P. Garnier, R. Modolo, J. Cui, M. Galand, and I. Müller-Wodarg (2009), On the ionospheric structure of Titan, *Planet. Space Sci.*, *57*, 1821–1827, doi:10.1016/j.pss.2009.04.012.

Ajello, J. M., J. Gustin, I. Stewart, K. Larsen, L. Esposito, W. Pryor, W. McClintock, M. H. Stevens, C. P. Malone, and D. Dziczek (2008), Titan airglow spectra from the Cassini Ultraviolet Imaging Spectrograph: FUV disk analysis, *Geophys. Res. Lett.*, *35*, L06102, doi:10.1029/2007GL032315.

Backes, H., et al. (2005), Titan's magnetic field signature during the first Cassini encounter, *Science*, *308*, 992–995, doi:10.1126/science.1109763.

Bird, M. K., R. Dutta-Roy, S. W. Asmar, and T. A. Rebold (1997), Detection of Titan's ionosphere from Voyager 1 radio occultation observations, *Icarus*, *130*, 426–436, doi:10.1006/icar.1997.5831.

Coates, A. J., F. J. Crary, G. R. Lewis, D. T. Young, J. H. Waite Jr., and E. C. Sittler Jr. (2007), Discovery of heavy negative ions in Titan's ionosphere, *Geophys. Res. Lett.*, *34*, L22103, doi:10.1029/2007GL030978.

Crary, F. J., B. A. Magee, K. Mandt, J. H. Waite Jr., J. Wastlake, and D. T. Young (2009), Heavy ions, temperatures and winds in Titan's ionosphere: Combined Cassini CAPS and INMS observations, *Planet. Space Sci.*, *57*, 1847–1856, doi:10.1016/j.pss.2009.09.006.

Cravens, T. E., J. Vann, J. Clark, J. Yu, C. N. Keller and C. Brull (2004), The ionosphere of Titan: An updated theoretical model, *Adv. Space Res.*, *33*, 212–215, doi:10.1016/j.asr.2003.02.012.

Cravens, T. E., et al. (2005), Titan's ionosphere: Model comparisons with Cassini Ta data, *Geophys. Res. Lett.*, *32*, L12108, doi:10.1029/2005GL023249.

Cravens, T. E., I. P. Robertson, S. A. Ledvina, D. Mitchell, S. M. Krimigis, and J. H. Waite Jr. (2008), Energetic ion precipitation at Titan, *Geophys. Res. Lett.*, *35*, L03103, doi:10.1029/2007GL032451.

Cravens, T. E., et al. (2009), Model-data comparisons for Titan's nightside ionosphere, *Icarus*, *199*, 174–188, doi:10.1016/j.icarus.2008.09.005.

Cui, J., et al. (2009a), Analysis of Titan's neutral upper atmosphere from Cassini Ion Neutral Mass Spectrometer measurements, *Icarus*, *200*, 581–615, doi:10.1016/j.icarus.2008.12.005.

Cui, J., M. Galand, R. V. Yelle, V. Vuitton, J.-E. Wahlund, P. P. Lavvas, I. C. F. Müller-Wodarg, T. E. Cravens, W. T. Kasprzak, and J. H. Waite Jr. (2009b), Diurnal variations of Titan's ionosphere, *J. Geophys. Res.*, *114*, A06310, doi:10.1029/2009JA014228.

Cui, J., M. Galand, R. V. Yelle, J.-E. Wahlund, K. Ågren, J. H. Waite Jr., and M. K. Dougherty (2010), Ion transport in Titan's upper atmosphere, *J. Geophys. Res.*, *115*, A06314, doi:10.1029/2009JA014563.

English, M. A., L. M. Lara, R. D. Lorenz, P. R. Ratcliff and R. Rodrigo (1996), Ablation and chemistry of meteoric materials in the atmosphere of Titan, *Adv. Space Res.*, *17*, 157–160, doi:10.1016/0273-1177(95)00774-9.

Galand, M., R. V. Yelle, A. J. Coates, H. Backes, and J.-E. Wahlund (2006), Electron temperature of Titan's sunlit ionosphere, *Geophys. Res. Lett.*, *33*, L21101, doi:10.1029/2006GL027488.

Galand, M., L. Moore, B. Charnay, I. Mueller-Wodarg, and M. Mendillo (2009), Solar primary and secondary ionization at Saturn, *J. Geophys. Res.*, *114*, A06313, doi:10.1029/2008JA013981.

Geppert, W. D., et al. (2004), Dissociative recombination of nitrile ions: $DCCCN^+$ and $DCCCND^+$, *Astrophys. J.*, *613*, 1302–1309.

Ip, W.-H. (1990), Meteoroid ablation processes in Titan's atmosphere, *Nature*, *345*, 511–512, doi:10.1038/345511a0.

Itikawa, Y. (2006), Cross sections for electron collisions with nitrogen molecules, *J. Phys. Chem. Ref. Data*, *35*, 31–53, doi:10.1063/1.1937426.

Kliore, A. J., et al. (2008), First results from the Cassini radio occultations of the Titan ionosphere, *J. Geophys. Res.*, *113*, A09317, doi:10.1029/2007JA012965.

Krasnopolsky, V. A. (2009), A photochemical model of Titan's atmosphere and ionosphere, *Icarus*, *201*, 226–256.

Lewis, G. R., et al. (2009), The calibration of the Cassini-Huygens CAPS Electron Spectrometer, *Planet. Space Sci.*, *58*, 427–436, doi:10.1016/j.pss.2009.11.008.

López-Moreno, J. J., et al. (2008), Structure of Titan's low altitude ionized layer from the Relaxation Probe onboard HUYGENS, *Geophys. Res. Lett.*, *35*, L22104, doi:10.1029/2008GL035338.

Ma, Y.-J., A. F. Nagy, T. E. Cravens, I. V. Sokolov, J. Clark, and K. C. Hansen (2004), 3-D global MHD model prediction for the first close flyby of Titan by Cassini, *Geophys. Res. Lett.*, *31*, L22803, doi:10.1029/2004GL021215.

Ma, Y., A. F. Nagy, T. E. Cravens, I. V. Sokolov, K. C. Hansen, J.-E. Wahlund, F. J. Crary, A. J. Coates, and M. K. Dougherty (2006), Comparisons between MHD model calculations and observations of Cassini flybys of Titan, *J. Geophys. Res.*, *111*, A05207, doi:10.1029/2005JA011481.

Ma, Y. J., et al. (2009), Time-dependent global MHD simulations of Cassini T32 flyby: From magnetosphere to magnetosheath, *J. Geophys. Res.*, *114*, A03204, doi:10.1029/2008JA013676.

McLain, J. L., V. Poterya, C. D. Molek, L. M. Babcock, and N. G. Adams (2004), Flowing afterglow studies of the temperature dependencies for dissociative recombination of O_2^+, CH_5^+, $C_2H_5^+$, and $C_6H_7^+$ with electrons, *J. Phys. Chem. A*, *108*, 6706–6708.

McLain, J. L., V. Poterya, C. D. Molek, D. M. Jackson, L. M. Babcock, and N. G. Adams (2005), $C_3H_3^+$ isomers: Temperature dependencies of production in the H_3^+ reaction with allene and loss by dissociative recombination with electrons, *J. Phys. Chem. A.*, *109*, 5119–5123.

Mendillo, M., P. Withers, D. Hinson, H. Rishbeth, and B. Reinisch (2006), Effects of solar flares on the ionosphere of Mars, *Science*, *311*, 1135–1138, doi:10.1126/science.1122099.

Michael, M., and R. E. Johnson (2005), Energy deposition of pickup ions and heating of Titan's atmosphere, *Planet. Space Sci.*, *53*, 1510–1514, doi:10.1016/j.pss.2005.08.001.

Modolo, R., and G. M. Chanteur (2008), A global hybrid model for Titan's interaction with the Kronian plasma: Application to the Cassini Ta flyby, *J. Geophys. Res.*, *113*, A01317, doi:10.1029/2007JA012453.

Molina-Cuberos, G. J., H. Lammer, W. Stumptner, K. Schwingenschuh, H. O. Rucker, J. J. López-Moreno, R. Rodrigo, and T. Tokano (2001), Ionospheric layer induced by meteoric ionization in Titan's atmosphere, *Planet. Space Sci.*, *49*, 143–153, doi:10.1016/S0032-0633(00)00133-1.

Mueller-Wodarg, I. C. F., R. V. Yelle, M. Mendillo, L. A. Young, and A. D. Aylward (2000), The thermosphere of Titan simulated by a global three-dimensional time-dependent model, *J. Geophys. Res.*, *105*, 20,833–20,856.

Nagy, A. F., and T. E. Cravens (1998), Titan's ionosphere: A review, *Planet. Space Sci.*, *46*, 1149–1155.

Neupert, W. M. (2006), Variability of the solar soft X-ray irradiance (0.6–2.5 nm) with solar activity, *Adv. Space Res.*, *37*, 238–245, doi:10.1016/j.asr.2005.01.072.

Rees, M. H. (1989), *Physics and Chemistry of the Upper Atmosphere*, Cambridge Univ. Press, New York.

Robertson, I. P., et al. (2009), Structure of Titan's ionosphere: Model comparisons with Cassini data, *Planet. Space Sci.*, *57*, 1834–1846, doi:10.1016/j.pss.2009.07.011.

Semaniak, J., et al. (2001), Dissociative recombination of $HCNH^+$: Absolute cross-sections and branching ratios, *Astrophys. J. Suppl. Ser.*, *135*, 275–283.

Shah, M. B., C. J. Latimer, E. C. Montenegro, O. J. Tucker, R. E. Johnson, and H. T. Smith (2009), The implantation and interactions of O^+ in Titan's atmosphere: Laboratory measurements of collision-induced-dissociation in N_2 and the modeling of positive ion formation, *Astrophys. J.*, *702*, 1947–1954, doi:10.1088/0004-637X/703/2/1947.

Shemansky, D. E., and X. Liu (2005), Evaluation of electron impact excitation of N_2 $X\ ^1\Sigma_g^+(0)$ into the N_2^+ $X\ ^2\Sigma_g^+(v)$, $A\ ^2\Pi_u(v)$, and $B\ ^2\Sigma_u^+(v)$ states, *J. Geophys. Res.*, *110*, A07307, doi:10.1029/2005JA011062.

Simon, S., U. Motschmann, G. Kleindienst, J. Saur, C. L. Bertucci, M. K. Dougherty, C. S. Arridge, and A. J. Coates (2009), Titan's plasma environment during a magnetosheath excursion: Real-time scenarios for Cassin's T32 flyby from a hybrid simulation, *Ann. Geophys.*, *27*, 669–685.

Tian, C., and C. R. Vidal (1998), Electron impact ionization of N_2 and O_2: Contributions from different dissociation channels of multiply ionized molecules, *J. Phys. B At. Mol. Opt. Phys.*, *31*, 5369–5381.

Tseng, W.-L., W.-H. Ip, and A. Kopp (2008), Exospheric heating by pickup ions at Titan, *Adv. Space Res.*, *42*, 54–60, doi:10.1016/j.asr.2008.03.009.

Vigren, E., M. Kaminska, M. Hamberg, V. Zhaunerchyk, R. D. Thomas, M. Danielsson, J. Semaniak, P. U. Andersson, M. Larsson, and W. D. Geppert (2008), Dissociative recombination of fully deuterated protonated acetonitrile, CD_3CND^+: Product branching fractions, absolute cross section and thermal rate coefficient, *Phys. Chem. Chem. Phys.*, *10*, 4014–4019.

Vigren, E., M. Hamberg, V. Zhaunerchyk, M. Kaminska, R. D. Thomas, M. Larsson, T. J. Millar, C. Walsh, and W. D. Geppert (2009), The dissociative recombination of protonated acrylonitrile, CH_2CHCNH^+, with implications for the nitrile chemistry in dark molecular clouds and the upper atmosphere of Titan, *Astrophys. J.*, *695*, 317–324, doi:10.1088/0004-637X/695/1/317.

Vuitton, V., R. V. Yelle, and M. J. McEwan (2007), Ion chemistry and N-containing molecules in Titan's upper atmosphere, *Icarus*, *191*, 722–742, doi:10.1016/j.icarus.2007.06.023.

Vuitton, V., R. V. Yelle, and J. Cui (2008), Formation and distribution of benzene on Titan, *J. Geophys. Res.*, *113*, E05007, doi:10.1029/2007JE002997.

Wahlund, J.-E., et al. (2005), Cassini measurements of cold plasma in the ionosphere of Titan, *Science*, *308*, 986–989, doi:10.1126/science.1109807.

Wahlund, J.-E., et al. (2009), On the amount of heavy molecular ions in Titan's ionosphere, *Planet. Space Sci.*, *57*, 1857–1865, doi:10.1016/j.pss.2009.07.014.

Waite, J. H., Jr., D. T. Young, T. E. Cravens, A. J. Coates, F. J. Crary, B. Magee, and J. Westlake (2007), The process of tholin formation in Titan's upper atmosphere, *Science*, *316*, 870–875, doi:10.1126/science.1139727.

Woods, T. N., (2008), Recent advances in observations and modeling of the solar ultraviolet and X-ray spectral irradiance, *Adv. Space Res.*, *42*, 895–902, doi:10.1016/j.asr.2007.09.026.

Yelle, R. V., J. Cui, and I. C. F. Mueller-Wodarg (2008), Methane escape from Titan's atmosphere, *J. Geophys. Res.*, *113*, E10003, doi:10.1029/2007JE003031.

Young, D. T., et al. (2004), Cassini plasma spectrometer investigation, *Space Sci. Rev.*, *114*, 1–112.

A. Coates and A. Wellbrock, Mullard Space Science Laboratory, University College London, Surrey RH5 6NT, UK.

J. Cui and M. Galand, Space and Atmospheric Physics Group, Department of Physics, Imperial College London, Prince Consort Road, London SW7 2AZ, UK. (m.galand@imperial.ac.uk)

V. Vuitton, Laboratoire de Planétologie de Grenoble, Université Joseph Fourier, F-38041 Grenoble, France.

J.-E. Wahlund, Swedish Institute of Space Physics, Box 537, SE-751 21 Uppsala, Sweden.

R. Yelle, Lunar and Planetary Laboratory, University of Arizona, 1629 E. University Blvd., Tucson, AZ 85721, USA.